Energy 147 (2018) 94–109

Contents lists available at ScienceDirect

Energy

journal homepage: www.elsevier.com/locate/energy

An experimental study on the aerodynamic performances and wake characteristics of an innovative dual-rotor wind turbine

Zhenyu Wang Graduate student [1], Ahmet Ozbay Graduate student, Wei Tian Postdoctoral associate, Hui Hu Professor *

Department of Aerospace Engineering, Iowa State University, Ames, IA 50011, USA

ARTICLE INFO

Article history:
Available online 5 January 2018

Keywords:
Horizontal-axis wind turbine (HAWT)
Dual-rotor wind turbine (DRWT)
Wake characteristics
Particle image velocimetry (PIV) measurements
Aerodynamic forces
Power outputs

ABSTRACT

A novel dual-rotor wind turbine (DRWT) concept with an auxiliary upwind rotor and a bigger downwind rotor was introduced for improved turbine performance. An experimental study was performed in an Atmospheric Boundary Layer (ABL) wind tunnel with scaled turbine models to investigate the aerodynamic performances and wake characteristics of DRWTs in either co-rotating or counter-rotating configuration (i.e., CR-DRWT or CO-DRWT), in comparison to those of a conventional single-rotor wind turbine (SRWT). In additional to measuring the aerodynamic forces and power outputs, the wake flow characteristics behind DRWTs and SRWT were also quantified by using a high-resolution Particle Image Velocimetry (PIV) system. In comparison to those of SRWT, while the aerodynamic force acting on the CR-DRWT was found to increase 13.3%, the power coefficient of the CR-DRWT design was improved by 7.2%. Faster wake recovery behind the DRWT designs was confirmed from both the measured power outputs of the same turbine model sited in the turbine wakes and the measured flow velocity at various downstream locations. The wake flow measurements were correlated with the aerodynamic force and power output data to elucidate underlying physics for the higher efficiency of DRWT designs in either isolation or wind farm settings.

1. Introduction

Conventional utility-scale horizontal-axis wind turbine (HAWT) configuration only has one singular rotor with three rotating blades mounted in front of turbine tower. Normally, while the rotating blades are optimized in the outboard sections to achieve high aerodynamic performance, the sections near the blade root region (approximately 25% of the inboard section) are mainly designed to support structural loads such as bending and torsion forces. Thus, the airfoils with extremely high ratio of thickness, but with inferior aerodynamic performance, are used in this section, resulting in a region near the blade root where virtually little to no wind energy is harvested from the oncoming flow. According to Betz limit, the theoretical maximum power coefficient can be achieved to 0.593 for a traditional HAWT with one singular rotor and with the assumptions of no viscous and swirling losses and infinite rotating blades. However, for a typical utility-scale HAWT, the maximum power coefficient (C_P) was measured to be in the range of 0.45–0.50 in field measurements [1]. There are several significant reasons to cause the difference between the theoretical Betz limit and the maximum power output in field tests, and one of which is the flow losses incurred in the blade root regions. Rosenberg et al. [2] found that the separations occurred in the blade root region would induce cross flows in spanwise direction, which would affect the flow performance of blade outboard sections. Sharma and Frere [3] stated that up to 5% loss in power generation is estimated for HAWT to compromise the rotor structural integrity. The root loss is massive, especially compared with the tremendous electricity generated every year (By the end of 2016, the global cumulative installed wind power capacity expanded to 486,749 MW) [4] from the large-scale onshore and offshore wind turbines.

As we know that, utility-scale wind turbines in modern wind farms are deployed as clusters instead of operating in isolated condition. Therefore, the wake interactions between upstream and downstream wind turbines in large-scale wind farms were found to result in substantial power losses ranging from 8% to 40% [5]. According to the suggestions by Vermeer et al. [6], the wake behind

* Corresponding author.
E-mail address: huhui@iastate.edu (H. Hu).
[1] Simulation Innovation and Modeling Center (SIMCenter), The Ohio State University, Columbus, OH 43210, USA.

https://doi.org/10.1016/j.energy.2018.01.020
0360-5442/

Nomenclature

A	Area of blade rotational disk [m^2]
C_M	Bending moment coefficient [−]
C_P	Power coefficient [−]
C_T	Thrust coefficient [−]
d	Diameter of the auxiliary rotor [m]
D	Diameter of the main rotor [m]
H	Turbine hub height [m]
I_u	Turbulence intensity [−]
P	Power output [W]
TSR	Tip-speed-ratio [−]
U_H	Freestream velocity at turbine hub height [m/s]
$\overline{u'w'}$	Reynolds stress [m^2/s^2]

Greek Letters

α	Power law exponent [°]
β	Turbine tilt angle [°]
ν	Kinetic viscosity of air [m^2/s]
σ_u	Root-mean-square of the turbulent velocity fluctuation [−]
η	Efficiency of DC generator [−]
ω_y	Vorticity (out of plane) [1/s]

HAWTs can be categorized into a near wake region and a far wake region. For the near wake region, generally, it refers to the location from the turbine rotational disk to the downstream distance about one diameter of the turbine rotor (D), where the flow features such as the evolution of unsteady blade tip and root vortices are primarily influenced by the actual shapes and the number of turbine blades. While a far wake region is located downstream behind the near wake, the flow characteristics are less complicated to its counterpart. In the past two decades, the HAWT wake characteristics have been extensively investigated by using experimental and computational methods. For examples, Varshney [7], Krogstad et al. [8], Hashemi-Tari et al. [9], Gao et al. [10], Zhong et al. [11] and Zhang et al. [12] studied the flow characteristics such as the unsteady helical tip vortices and the separated flows around the rotor blades in the near wake. While the studies of far wake are mainly focused on investigating the effects such as wake interferences [13], topography [14] and turbulence models [15,16]. The massive power losses (also called wake losses) caused by the wake interferences from upstream and downstream wind turbines, were found to be significantly dependent of location and layout of wind farms as well as incoming flow conditions [17]. Adaramola et al. [18] found that the wind turbine spacing and the operating condition of the upstream turbine have significant effects on the performance reduction of the maximum C_P of downstream turbine. Barthelmie et al. [19] performed a field test at the Nysted offshore wind farm to evaluate the wind farm efficiency and wind turbine wake characteristics. They observed that wind speed variation was the dominant factor in wake losses, but the wind direction, turbulence intensity as well as atmospheric stability were deemed to be the lower order effects. Later, Hansen et al. [20] analyzed the statistical data of operational characteristics and power as well as meteorological measurements of wind turbines operating in Horns Rev offshore wind farm at Denmark. They found that the power deficit in the wind farm has an inversely proportional relationship with ambient turbulence intensity. They also stated the velocity deficits in wake regions would recover from 10% to 45% with the turbine spacing ranging from 1.7D to 7.4D. Chamorro et al. [21] found the effects of turbine wake can be extended as far as 20 rotor diameters to the downstream location, which is similar to the findings in the study of Zhang et al. [22]. Recently, Li et al. [23,24] performed both experimental and numerical investigations on power performance and wake characteristics for a HAWT, the results revealed that the incoming flow with a higher turbulence intensity is beneficial for velocity recovery in the turbine wake, which corresponds well with the results reported in Tian et al. [25].

Compared with the large amounts of researches conducted to predict and measure the losses in turbine wakes, relatively very little attention is paid in reducing the wake losses. In fact, with the concerns that the suitable sites (both onshore and offshore locations) can be practically used for installing wind turbines are going to exhaust in the near future, therefore, the research focus has switched to design more efficient wind turbines and wind farm layouts, aiming to harvest more wind energy from the same incoming flow conditions. As a result, dual-rotor wind turbine (DRWT) configuration was proposed to achieve a higher efficiency in harnessing more wind energy from incoming airflows [26]. Lee et al. [27,28] compared the power outputs of a traditional single-rotor wind turbine (SRWT) and an identical-sized dual-rotor wind turbine with counter-rotating (CR-DRWT) configuration. The measured results showed that the power coefficient of the CR-DRWT was improved by 30% in comparison to that of a SRWT with only half solidity, but was 5% lower than a SRWT having the same solidity. Later, Ozbay et al. [29] performed an experimental investigation on a DRWT with co- and counter-rotating configurations operating in isolated conditions, they found the counter-rotating design could harvest more energy than the co-rotating configuration from the same incoming wind, which also confirms the findings reported in Yuan et al. [30]. However, these previous dual-rotor designs were mainly focused on extracting more wind energy by adding more rotor blades rather than reducing the flow losses existed in the wake or root region to achieve a higher efficiency. These strategies may be effective for a turbine operating in isolated conditions but have essential negative effects on downstream turbines if they are placed in wind farm scenarios due to the substantial velocity deficits in the wake. As described in Barthelmie and Jensen [31], 1% enhancement of power generation in a 100 MW wind farm would contribute an extra revenue of half million dollars per year. Therefore, the losses in turbine wakes and in root region of turbine rotors should be considered as key factors affecting the efficiency of individual wind turbines and large-scale wind farms.

In the present study, an innovative DRWT, with a small rotor amended in front of the main rotor using by different shafts, was designed to improve the power efficiency of HAWT operating in isolated conditions and in wind farm scenarios. The improvement of power generation for individual wind turbines was achieved by reducing the aerodynamic losses caused in the root regions and the enhancement of efficiency in wind farms was attained by promoting the turbulent mixing of wake flows to reduce wake losses. Two configurations with co- and counter-rotating designs for the upwind and downwind turbines were quantitatively measured in comparison to a conventional SRWT system. The instantaneous wind loads acting on the miniature wind turbines were measured to quantify the force analysis. The detailed velocity measurements, including point-wise and planar fields, were measured by employing an intrusive (Cobra-probe) methodology and a non-intrusive (Particle Image Velocimetry, PIV) technique, respectively, under the same incoming flow condition. The measured velocity and vorticity distributions were employed to characterize the turbine wake characteristics and evolutions of the unsteady blade tip and root vortices. The power outputs of isolated wind turbines (i.e., SRWT, CO-DRWT and CR-DRWT models) and a same

model turbine placed at various downstream distances were measured to quantify the flow performance for individual turbines and the velocity recovery characteristics behind the turbine wakes.

2. Experimental setup and wind turbine models

2.1. Wind-tunnel

The experimental measurements were performed in a large-scale Atmospheric Boundary Layer (ABL) wind tunnel with the dimension of 20.0 m × 2.4 m × 2.3m in the test section. It is a closed-circuit wind tunnel with the capacity of generating a maximum ABL wind speed of 45 m/s. The side walls in the test section are transparent, which is very convenient to perform optical tests such as PIV measurements. Fig. 1 shows a picture of the test section of the wind tunnel where a conventional miniature HAWT model was mounted at the center of the wind tunnel ground. A series of aluminum chain arrays, which are perpendicular to the flow direction (i.e., *x*-direction) and with an equal spacing of 15-inch, were placed on the ground of test section in order to generate an incoming airflow with an ABL wind profile usually seen in offshore wind farm scenario. The wind tunnel ceiling can be adjusted along the streamwise direction to ensure the boundary layer growth of the simulated wind profile under approximate zero pressure gradient in the streamwise direction. Further information of this wind tunnel in generating ABL wind profiles can be found in the previous study of Tian et al. [25].

It is suggested that a typical wind profile over an open terrain condition can be expressed by applying an approximate power law function. In this study, the profile of the incoming airflow speed in vertical direction ($U(z)$) can be expressed as a power law function based on the velocity at the turbine hub height (H) [32]:

$$U(z) = U_H(z/H)^{\alpha} \tag{1}$$

where U_H is the speed of incoming airflow at the turbine hub height H and the value of the exponent 'α' in this equation is determined by different surface roughness. As we know that, due to the ocean surface is quite flat, offshore wind farms have relatively lower turbulence levels in the oncoming airflows compared to those sited on onshore terrains. Turbines operated in typical offshore wind farms (e.g., the Greater Gabbard in UK and Horns Rev II in Denmark) are usually facing an ABL wind profile with the exponent of α near 0.10 [20]. Besides, Hsu et al. [33] recommended an exponent α of 0.11 for open sea terrains under neutral stability condition, which is similar to the value recommended by ISO standard [17]. Then, for the turbulence intensity of incoming airflows, Tong [34] suggested a range from 8% to 12% that is usually used at the hub height of offshore wind turbines to represent typical incoming flow variations. Fig. 2 shows the wind profiles used for the current study, including wind speed and turbulence intensity at variant heights, which were measured at the location where the test model turbines were mounted by using a high-resolution anemometry system. It should be noted that the streamwise velocity shown in Fig. 2(a) is normalized by the streamwise velocity at the turbine hub height (U_H). By adjusting the ceiling height of the wind tunnel, the incoming wind speed fitted quite well to a power law plot with the exponent of $\alpha = 0.11$. The turbulence intensity was also accordingly set to 9.9% at the turbine hub height. In this test, the turbulence intensity (I_u) is defined as follows:

$$I_u = \sigma_u / \overline{U}_{local} \tag{2}$$

where σ_u is the root-mean-square of the streamwise velocity fluctuation, and $\overline{U}_{local}$ is the time-averaged velocity where the anemometer was located. Both of the wind speed and the turbulence intensity profiles are time-averaged results based on 120 s measurement, and which are suitably located within the range as suggested by Hsu et al. [33] and Tong [34].

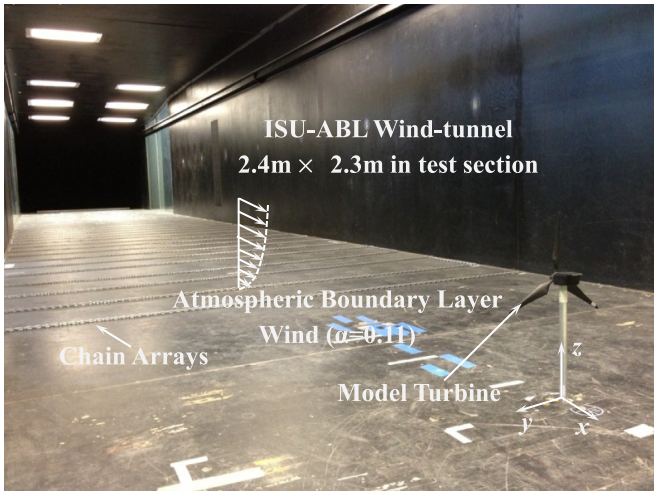

Fig. 1. Test section of the wind-tunnel and a conventional miniature wind turbine mounted on the ground.

2.2. Wind turbine models

In this study, three miniature model wind turbines (SRWT, CO-DRWT and CR-DRWT) were constructed for the comparative investigations. The SRWT represents the most extensively used three-blade HAWT deployed in large-scale wind farms, which is also utilized as the baseline model in this experimental test [35]. Fig. 3 shows the schematic of the three model wind turbines used in the current study. Fig. 3(a) illustrates a conventional SRWT model, which has a tilt angle (β) of 5° for the rotor. The cross sections (i.e., airfoil shape) of rotor blades are the same as the platform profiles using in ERS-100 turbine blades developed by TPI Composites [25]. Three NREL airfoils, S821, S819 and S820, are utilized from root to tip sections with a smooth transition in spanwise direction. While as a contrast with this baseline, the DRWT model employs an auxiliary small rotor, appending upwind of the main rotor (by separated shaft). The configurations of the small rotor are same with the big rotor, but the size was scaled down to half. The DRWT model with two configurations, co-rotating (Fig. 3(b)) and counter-rotating (Fig. 3(c)), were adopted to find the impact of relative rotation direction between the upwind and downwind turbines. It should be mentioned that in the DRWT designs, the rotational direction is kept as the same for the upwind auxiliary rotor, only the downwind main rotor is shifted in different configurations. The diameters of the main rotor (D) and auxiliary rotor (d) are 0.28m and 0.15m, respectively. The height of the turbine hub (H), namely, the distance between the ground and the turbine hub, is 0.225m for all model turbines. The distance between the rotational disk of the upwind and the downwind rotors in the DRWT systems is 0.25D (0.07m). The model turbines (with a scaled ratio of 1:320) are designed to mimic a conventional utility-scale HAWT with the rotor diameter of 90m and turbine hub height of 80m sited in the typical offshore wind farms. The rotating blades, hubs and nacelles, are fabricated through a rapid prototyping machine by using stiff plastic materials. The blockage ratio in the test section is calculated to be around 1.2%, thus, the blockage effect can be omitted in the measurements [36].

During the test, these miniature wind turbines were mounted at

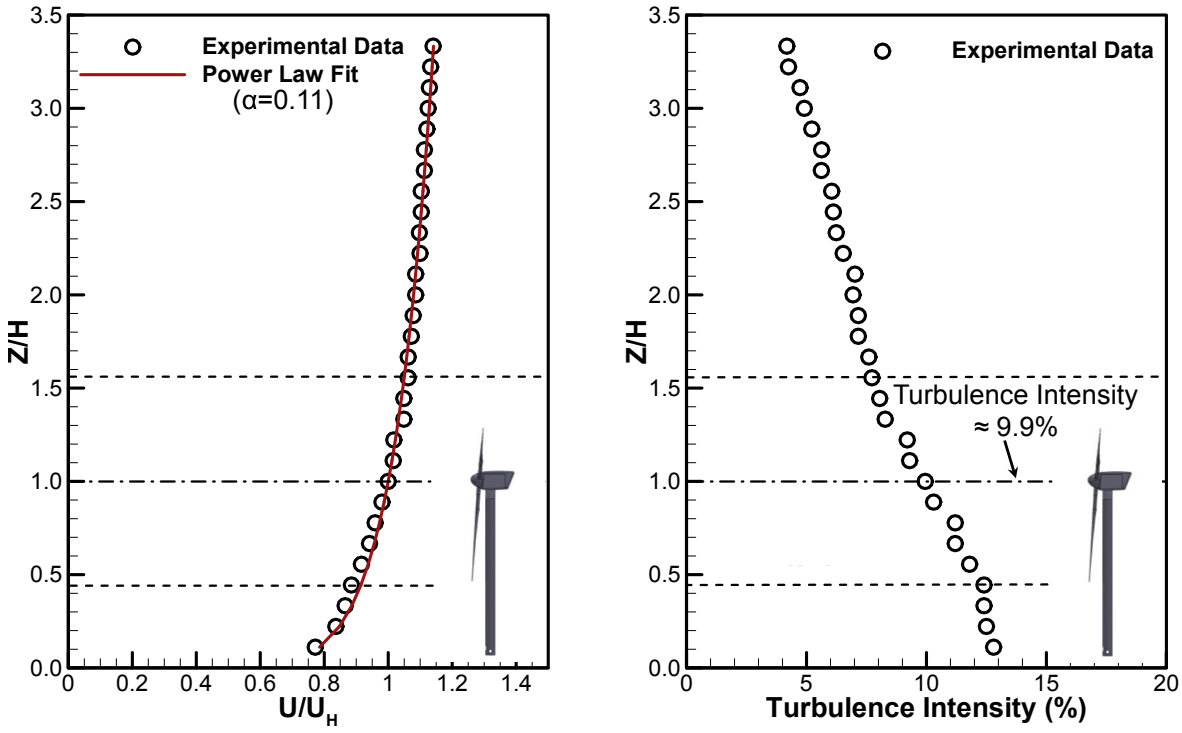

(a) Streamwise velocity profile (b) Turbulence intensity profile

Fig. 2. ABL wind profiles used in the experiments.

the ground center in test section. The streamwise velocity at the height of turbine hub was adjusted to be about 6.5 m/s ($U_H = 6.5$ m/s). Therefore, based on the diameter of the main rotor and this velocity, the corresponding Reynolds number ($Re_D = U_H D/\nu$) was calculated to be around 1.2×10^5. Obviously, this value is essentially lower than those in utility-scale HAWTs ($Re_D > 1.2 \times 10^7$) operated in large-scale wind farms [37]. According to previous researches, such a low Reynolds number may have a vital impact on the power performance of HAWTs, because the boundary layer flow over rotating blades are known to be highly sensitive to Reynolds numbers [38,39]. However, based on the study performed by Chamorro et al. [40], the flow characteristics in turbine wakes such as mean velocity, shear stress and turbulence intensity illustrated asymptotic manners with the changing of Reynolds numbers. The independence of Reynolds number for mean velocity was found to be reached at lower values ($Re_D \approx 4.8 \times 10^4$) in comparison to those of higher order quantities. While the higher order characteristics such as shear stress and turbulence intensity started at $Re_D \approx 9.3 \times 10^4$. As mentioned above, the Reynolds number in this study is around 1.2×10^5, which lies above the minimum requirement of Reynolds number independence as suggested by Chamorro. Similarly, from the studies of Whale et al. [39] and Medici et al. [41], the behaviors of the unsteady flow structures in the turbine wake would become approximately independent to Reynolds numbers once it reached to a certain level. They also stated that the wind turbines would generate similar unsteady flow structures such as the shape and rotational direction of tip vortices under the same tip-speed-ratio (TSR).

2.3. Dynamic wind load and power output measurements

During the experiment, the wind turbine blades, hub and nacelle were assembled together and supported by a circular aluminum rod that was employed as a turbine tower. In order to obtain the aerodynamic forces acting on the model wind turbines operated in a stable condition, a JR3 load cell (model: 30E12A-I40) with a measurement uncertainty levels less than ±0.25% of the full force range (40N) shown in Fig. 4, was applied to measure the dynamic thrust forces and bending moments through a high-sensitive force transducer. The details about this load cell can be found in our previous research [17]. It was mounted under the wind tunnel test section and also used to support the turbine tower. During the measurements, the data of aerodynamic forces acting on these model turbines were collected for 120 s at a sampling rate of 1000 Hz for each model wind turbine. A Monarch tachometer was adopted to capture the turbine rotational speeds. It should be noted that the resonant frequencies measured from the load cell were found to be essentially higher than the rotational frequencies of turbine rotors.

The power outputs of these miniature wind turbines can be calculated through measuring the voltages from the DC generators in the nacelles and the currents in the electric circuits. The optimum TSR (i.e., with the maximum power output) was observed to be around 5.0 in the current study, which lies in the range of 4.0–8.0 for typical modern wind farms [1].

2.4. Flow field measurements

Fig. 4 also shows the experimental setup for the 2-D PIV measurements, which was employed to measure the velocity fields at the central plane (i.e., $Y = 0$) to quantify the flow characteristics in the wake flows ($X/D < 2.2$). A fog machine (ROSCO 1900) was used to generate small oil droplets (about 1 μm in diameter) and spray them in the incoming airflow for illumination purpose. A double-pulsed Nd:YAG laser (EverGreen 200) was utilized to generate a pulsed laser beam at a wavelength of 532 nm. The laser beam was

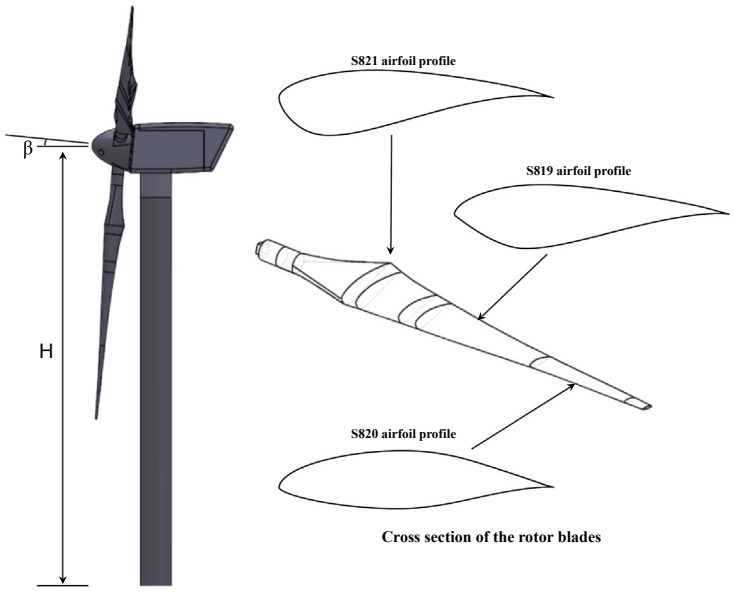

(a) SRWT model

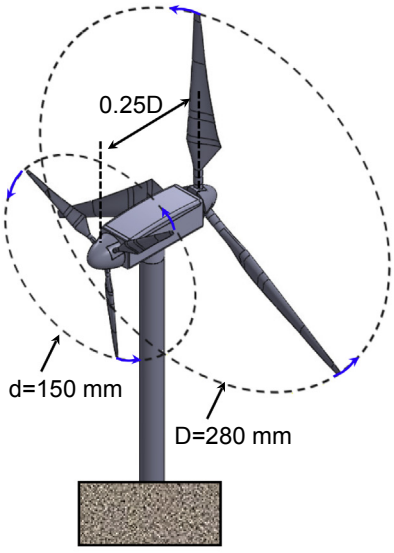

(b) CO-DRWT model

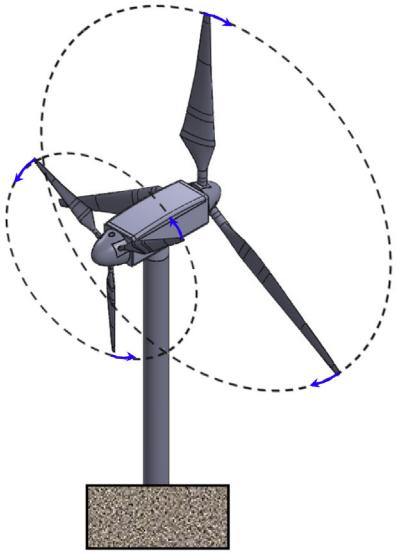

(c) CR-DRWT model

Fig. 3. Wind turbines used in this study.

then formed as a sheet with a thickness of around 1.0 mm after passing through a series of mirrors along with cylindrical and spherical lenses. Two high-resolution 14-bit CCD camera (PCO2000) were placed perpendicular to the laser sheet and deployed for image acquisitions, because the capture window of one camera is not sufficient to visualize the whole interested region in the near wake. As a result, two CCD cameras, with an overlapping area of 20 mm in streamwise direction, were used to capture the snapshots of whole interested wake region simultaneously. A digital time delay generator (BNC565) was applied to control the timing sequences of the laser system and the snapshot acquisition. The detailed connections among the camera, laser and delay generator can be found in Fig. 4. After the image acquisition, the instantaneous velocity components were derived from the measured PIV snapshots in the post-processing by using a cross-correlation with an interrogation window of 32×32 pixels and an effective overlap rate of 50%. The ensemble-averaged flow characteristics such as mean velocity, vorticity and Reynolds stress can be calculated from the velocity components and their variances. For each test case, a sequence of 1000 pairs of instantaneous images were captured to attain a good convergence of flow characteristics of the ensemble-averaged measurements. The measurement uncertainty level was estimated to be around 2% for velocity and 5% for the vorticity and Reynolds stress [42].

In order to obtain the time-averaged and instantaneous flow details, both ensemble-averaged and phase-locked PIV measurements were performed. During the ensemble-averaged measurements, a constant image acquisition rate (different from the blade rotating frequency) was utilized to measure the flow quantities in the wake region under as much blade phase angles as possible. While for the phase-locked measurements, a digital tachometer and another time delay generator (Stanford DG535) were amended

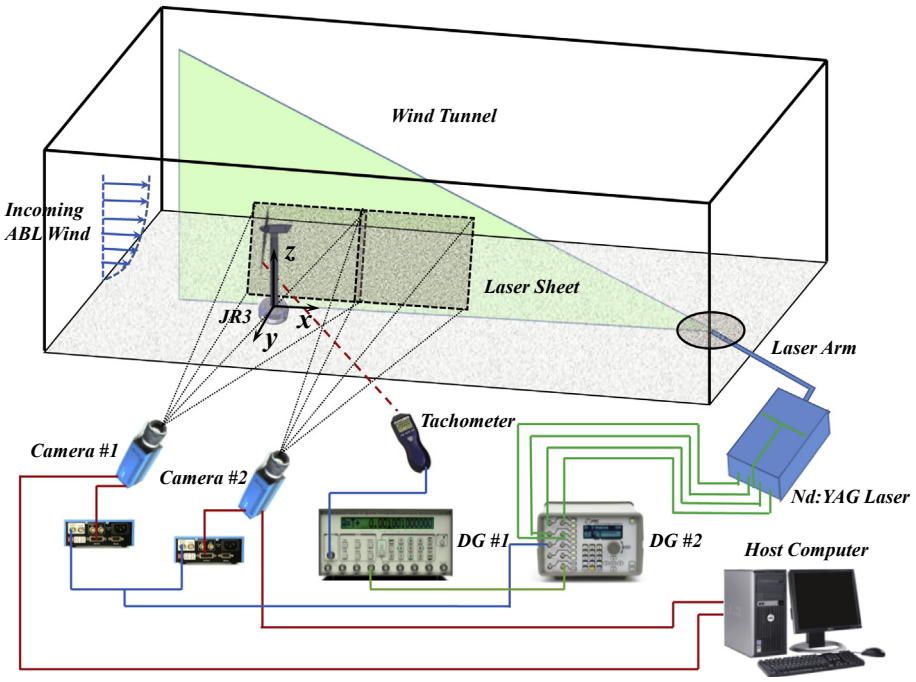

Fig. 4. Experimental setup used for the aerodynamic forces and PIV measurements.

in the system to control the image acquisition at a specific blade phase position. They were performed to elucidate more insights about the evolution of unsteady turbulent structures such as tip and root vortices shedding from different blade phase positions. During the measurement, the zero phase angle was pre-selected at the most upward position of a rotor blade, which was also marked by a reflective tape on the blade surface. 8 blade phase angles were selected ranging from 0° to 105° with an increment of 15°. For each selected blade phase angle, 400 image pairs were captured to calculate the phase-averaged flow statistics in the wake regions.

In addition to the 2-D PIV measurements, an anemometer called cobra probe (TFI Series 100), was also used to measure the mean and fluctuating point-wise flow velocities (x, y and z direction) in the central plane at the far wake regions ($X/D = 2.0$, 4.0, 6.0, 8.0 and 12.0), which were also employed to supplement the 2-D PIV measurements in the near wake region and obtain the information of wake recovery. For each selected position, the data acquisition was acquired for 120 s (2-min) at a sampling rate of 1,000 Hz to achieve a good convergence.

3. Results and discussion

3.1. Measurements of aerodynamic forces acting on the wind turbines

The effects of aerodynamic forces acting on wind turbines have been attracting more and more attention in the optimal design of modern HAWTs [38]. In this study, the force measurements were conducted through a JR3 load cell that can be used to monitor instantaneous results of x, y and z force components and moments at 1,000 Hz. The thrust coefficient (C_T) and the bending moment coefficient (C_M) of the wind turbine models, are defined as follows [43]:

$$C_T = \frac{T_x}{\frac{1}{8}\rho U_H^2 \pi D^2} \tag{3}$$

and

$$C_M = \frac{M_z}{\frac{1}{8}\rho U_H^2 \pi D^2 H} \tag{4}$$

where T_x is the x-component of the thrust force (i.e., streamwise direction) acting on these miniature wind turbines, M_z is the bending moment along z direction and ρ is the density of incoming airflow. Fig. 5 illustrates the measured aerodynamic loads in terms of instantaneous thrust coefficients. The time-averaged data (denoted as the red dashed line) is depicted in the plot for comparison. It should be noted that only the thrust coefficient is reported in the plot because similar trend of bending moment coefficient is also observed in the measurements.

As can be seen clearly in Fig. 5, the time sequences of thrust acting on these model wind turbines are highly fluctuated during the measurements. Both of the mean thrust coefficient and its standard deviation (σ) values in the DRWT models (i.e., the CO- and CR-DRWT models) are found to be higher than those in the SRWT models, which can also be found in Table 1. As expected, the DRWT designs would induce higher values both in the mean and fluctuated aerodynamic forces on the turbine tower because of the small rotor appended in the wind turbine system. Due to the existence of the auxiliary rotor in the DRWT designs, the mean thrust loads are found to be increased by 13.3% and 3.5% for the CO- and CR-DRWT models, respectively. In comparison to the thrust coefficient, the bending moment in the DRWT systems is found to be less promoted (only 10.8% and 1.2% increase are observed in the CO- and CR-DRWT models, respectively). However, the standard deviation of the aerodynamic forces acting on the DRWT models are observed to augment substantially (66.7% enhancement in the thrust for the CO-DRWT and 14.6% increase for the CR-DRWT, and similar significant increases can be observed in the bending moment), compared with those measured in the SRWT case. As suggested by Hu et al. [38] and Tian et al. [25], the standard deviation values of aerodynamic forces can be utilized as a substantial parameter to evaluate the fatigue condition on wind turbines. The larger variations (i.e., with high standard deviations) of aerodynamic forces in the DRWT designs would indicate more significant fatigue loads

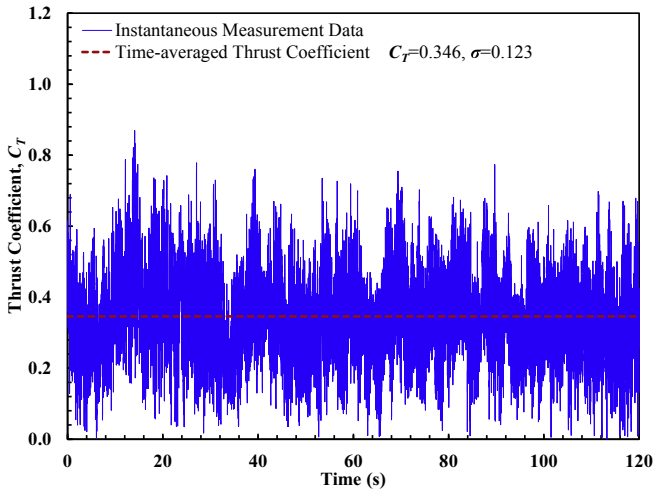

(a) SRWT model

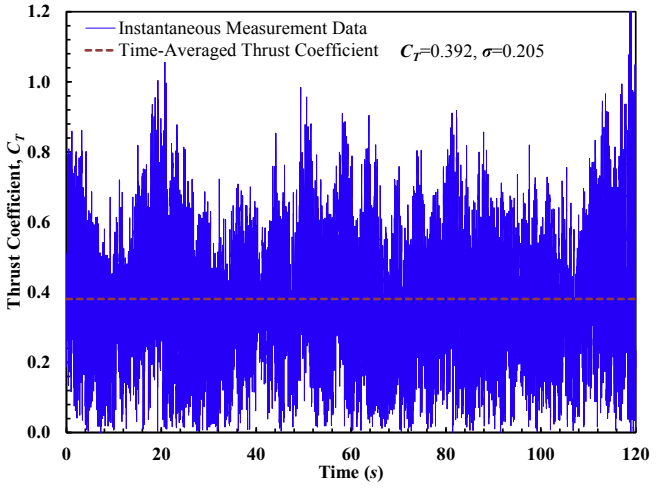

(a) CO-DRWT model

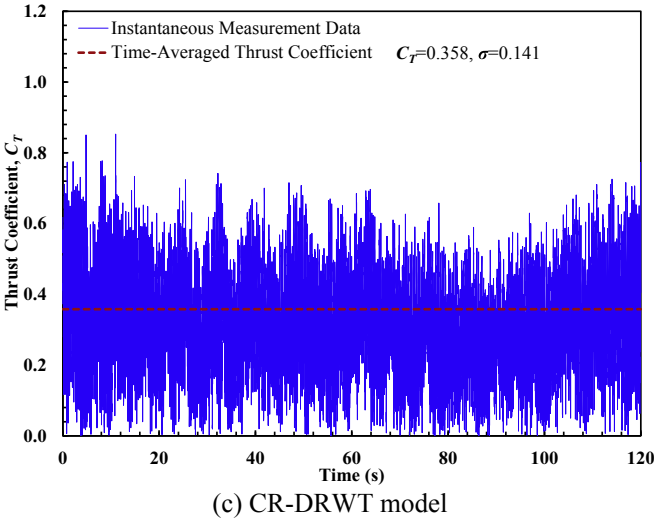

(c) CR-DRWT model

Fig. 5. Time history of the instantaneous thrust coefficient.

acting on the turbine tower, which is believed that the appended small rotor would generate complicated turbulent structures and enhance the turbulence intensity levels in the root region. As can be seen from the results, the relative rotation direction of dual-rotor configurations has essential impact on the aerodynamic forces acting on the turbines. The higher aerodynamic forces in the CO-DRWT case, including time-averaged and instantaneous results, may imply a stronger wake interference between the upwind and downwind rotors than that in the CR-DRWT design. Therefore, the forces acting on co-rotating configuration, are prominently larger than those on the counter-rotating design. However, a larger thrust doesn't imply a higher power output in the DRWT configurations. The characteristics of power output would be mainly determined by the complex flow structures and will be discussed in the following power measurements session.

Table 1
The aerodynamic forces acting on the SRWT and DRWT models.

	SRWT	CO-DRWT	CR-DRWT
Mean thrust coefficient, C_T	0.346	0.392	0.358
The standard deviation of the thrust coefficient, σ_{CT}	0.123	0.205	0.141
Mean bending moment coefficient, C_M	0.411	0.455	0.416
The standard deviation of the bending moment coefficient, σ_{CM}	0.133	0.242	0.165

3.2. Power measurements

The target of designing the DRWT system is trying to mitigate the root losses and enhance the wake mixing for a faster velocity recovery. First of all, in order to evaluate the benefit of DRWT designs for mitigating the root losses, the power output coefficients of isolated wind turbine models were measured for the comparison. As mentioned above, since the Reynolds number in such miniature wind turbines is much lower than that in the utility-scale wind farms, which has vital effect on the power generation in the wind-tunnel testing [38]. Therefore, the power coefficients of these model turbines (C_P) were normalized based on the measured power coefficient on the isolated SRWT system (C_{P_ref}), instead of comparing the absolute value of power coefficients directly. In the present study, the power coefficient is determined as follows [44]:

$$C_P = \frac{V^2\eta}{\frac{1}{2}\rho U_H^3 A R_L} \tag{5}$$

where R_L is the electric resistance applied in the circuit, V is the voltage measured on R_L, A is the rotational area of the main rotor and η is the efficiency of DC generator. For the SRWT model, only one DC generator was used in the nacelle, but two DC generators were used in the DRWT designs since there are two rotors installed at the upstream and downstream of turbine tower, respectively. Thus, the total power of DRWT configurations is the sum of the auxiliary rotor and the main rotor. In fact, the optimum mechanical power coefficient for the SRWT model was found to be around 0.2, which is much lower than that of large-scale HAWTs operated in modern offshore wind farms.

Fig. 6 presents the normalized power coefficients for the SRWT and DRWT models operating in isolated condition. C_{P_ref} is the reference power coefficient, which was measured on the baseline SRWT model used in the current study. It can be seen clearly that, both of the DRWT designs illustrate higher total power outputs compared with that in the SRWT system, indicating extra wind energy is harvested by the amended small rotor in the DRWT systems. As shown in the figure, only 1.8% total power increase is found in the co-rotating configuration but 7.2% enhancement is observed in the counter-rotating design. While in the DRWT configurations, the power generated from the auxiliary rotor accounts for about 11.8% of the total power outputs for both cases. Since a portion of wind energy is harnessed by the upstream small rotor, the power generation from the big rotor is found to be reduced by 10% and 4.3% for CO-DRWT and CR-DRWT models, respectively, in

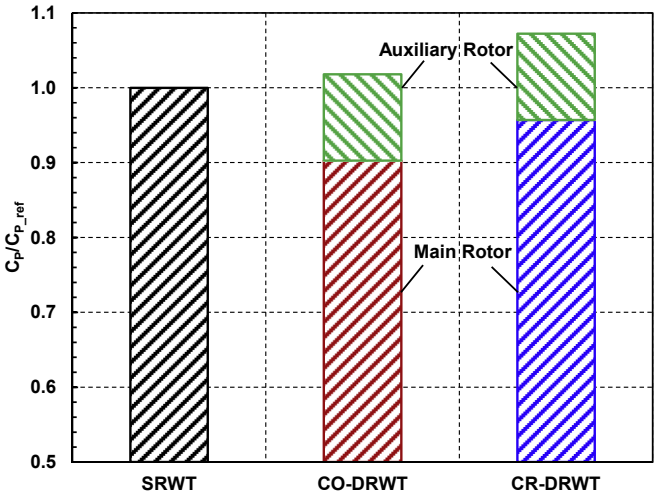

Fig. 6. Power measurement comparisons for the isolated SRWT and DRWT models.

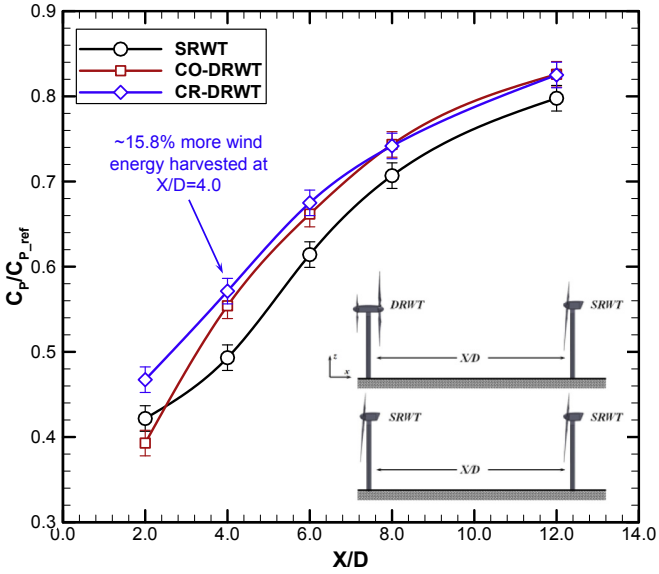

Fig. 7. Power measurement comparison for a same SRWT model sited in the downstream wakes.

comparison with that generated from the SRWT. This would indicate the counter-rotating configuration is a better option for harnessing more wind energy from the same incoming airflow. In fact, the portion of wind energy harvested by the small rotors in DRWT designs is the same, suggesting the differentiation would come from the downwind main rotor. Similar to the results of aerodynamic forces, the rotation directions play an important role in harnessing wind energy for different configurations. As the rotational directions of the rotors in co-rotating design are identical, the induced wake flow behind the auxiliary rotor may not be beneficial for enhancing the power output of the main rotor. However, this situation is inverse in the counter-rotating concept, as 5.4% more wind energy is found to be extracted from the same incoming wind. As a result, more insights behind the improvement of power harvest should be revealed and which will be discussed in the following flow field measurements.

As mentioned above, another target of the dual-rotor designs is to enhance the mixing in the wake flows, which aims to achieve a faster velocity recovery than that in the single-rotor case. Therefore, a series of power measurements were also performed to directly assess and compare the power outputs of the same wind turbine model placed at different downstream locations that aligned with the streamwise direction behind the SRWT and DRWT systems. It is also used to examine the effects of the spacing of turbines in wind farms as reported in Barthelmie et al. [45,46]. Similarly, the power outputs of the SRWT model sited in the wake flows were normalized as above. Fig. 7 depicts the normalized power coefficient of the same turbine placed in the wake flows in terms of variant distances away from the upstream wind turbines. The power outputs of the downstream SRWT were first measured at $X/D = 2.0$, and then were measured at other further locations (i.e., $X/D = 4.0$, 6.0, 8.0, and 12.0) when the turbine was moved downstream in the wake region. During the experiments, the upstream wind turbines were operating at their optimum conditions (i.e., with the highest power output).

We know that, the power losses in the wake region are caused by a large portion of wind energy harvested by upstream wind turbines. The power losses are found to be as high as around 60% when the downstream wind turbine was placed at $X/D = 2.0$ for the SRWT and the CO-DRWT models, and slightly over 53% in the case of CR-DRWT. This location can be approximately considered in the near wake region, where the wake losses are greatly affected due to the existence of upstream wind turbines. The results shown in Fig. 7 indicate that the wake losses in the CR-DRWT design are less than those in the other two model turbines at $X/D = 2.0$. Similar to the results discussed in the aforementioned dynamic force and power output measurements for isolated wind turbines, the relative rotation directions of the auxiliary rotor and the main rotor in DRWT designs have significant influence on the velocity recovery in the turbine wakes. The power output in the CO-DRWT design is about 6.8% lower than that in the SRWT model, while 10.8% higher can be seen in the CR-DRWT configuration. When the downstream turbine is moved to $X/D = 4.0$, an improvement of 15.8% can be observed in the case of CR-DRWT in comparison to the conventional SRWT case, which is the maximum enhancement at all the measurement locations from near wake to far wake regions (i.e., from $X/D = 2.0$ to $X/D = 12.0$). Meanwhile, the measured power output of the CO-DRWT model is found to be essentially augmented compared with that in the SRWT model at this location, where a 12.4% more power is measured in comparison to 6.8% less obtained at $X/D = 2.0$. Such a sharp improvement would imply a much faster increasing rate of velocity recovery in the wake of the CO-DRWT model. This result illustrates that the highest wake recovery speed shown in the CO-DRWT case would occur within the downstream region from $X/D = 2.0$ to 4.0, indicating more high-momentum airflows over the turbine wake are entrained to recharge the low-momentum flows in the turbine wakes.

From the power measurements in the wake regions, we can find that both of the co-rotating and counter-rotating configurations are beneficial for promoting power outputs for the wind turbine sited at downstream locations by enhancing the turbulent mixing in the wake regions. As the downstream turbine is moved to the location of $X/D = 6.0$, the benefits of dual-rotor designs are reduced slightly but still have about 10% more power outputs. As expected, the impact of turbulent mixing induced by the upwind and downwind rotors is found to be gradually alleviated as the downstream model turbine is moved further away from the upstream turbines. When the downstream turbine is placed at $X/D = 8.0$ and 12.0, the benefits of the dual-rotor designs are found to be abated greatly compared to those in the near region (e.g., $X/D = 4.0$). This result would be quite similar with the findings reported in Hansen et al. [20], they stated that if the spacing between upstream and downstream wind turbines exceeds 6.5D, the recovery of velocity deficits in the turbine wake is very slow. In addition, the effect of rotation direction for power output is observed to be disappeared eventually at $X/$

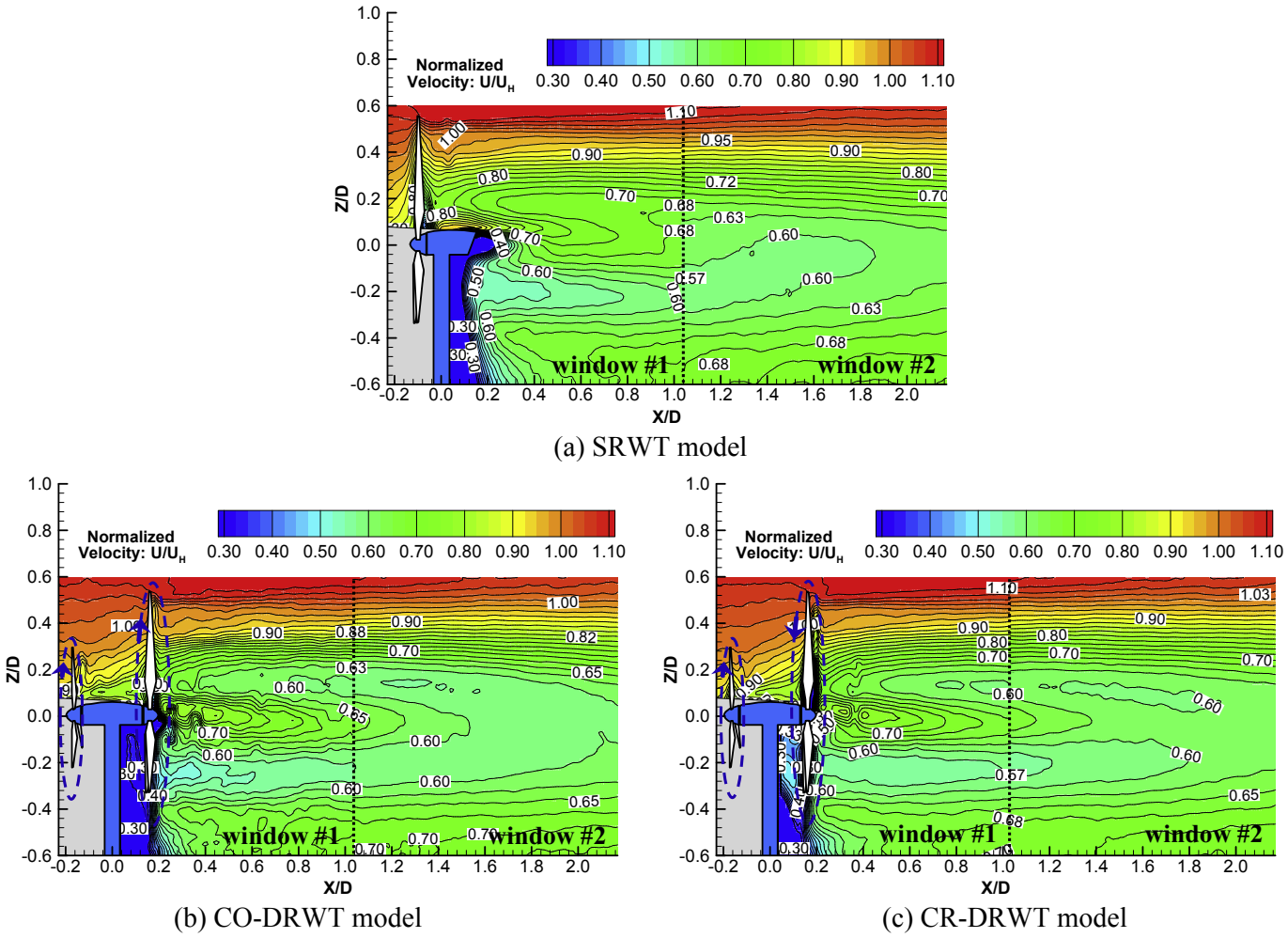

Fig. 8. Ensemble-averaged streamwise velocity distributions in the wake flows.

$D = 8.0$ in terms of the approximately identical results obtained from the measurements of CO-DRWT and CR-DRWT designs. According to the interpolation data from the relative power coefficient shown in Fig. 7, the power losses of the downstream wind turbine are calculated to be about 35%, 27% and 23%, at the locations of 7.0D, 9.4D and 10.5D, respectively, in the wake of the SRWT model. These values are found to agree very well with the field test data in the wake of a conventional wind turbine installed in Horns Rev offshore wind farm [5]. In fact, the upstream wind turbines employed for this wake recovery evaluation can be considered as the same condition of the isolated turbines measured in Fig. 6. As a result, with an auxiliary rotor installed in front of the main rotor, it would not only be able to harvest more energy for upstream turbines from the same incoming airflow (i.e., by reducing the losses in the root regions of the big rotor), but also be capable of mitigating the wake losses for downstream turbines (i.e., by enhancing the turbulent mixing in wake flows) in typical wind farm scenarios, in comparison to those of the SRWT model.

3.3. PIV measurement results

Fig. 8 illustrates the ensemble-averaged streamwise velocity distributions in the near wake region (up to $X/D = 2.2$) of the SRWT and DRWT models, which are normalized by the freestream velocity at the hub height (U_H). It should be noted that the blue arrows near the turbine blades represent the rotation directions of the auxiliary and main rotors in the CO-DRWT and CR-DRWT models. As mentioned in part of experimental setup for PIV measurements, the image capture window within one camera is not sufficient to capture the whole interested region, thus two cameras were employed in tandem to visualize the region ranging from $X/D = -0.2$ to $X/D = 2.2$ (the location of turbine tower is defined as $X/D = 0$). In Fig. 8, the results illustrated in window #1 are acquired from the first camera (i.e., the left side of the dashed line) and the rest shown in window #2 are acquired by the second camera (i.e., the right side of the dashed line). It can be seen that, significant velocity deficits are measured in the wake regions of all three wind turbine models, indicating a significant proportion of the kinetic energy from the incoming airflow is harnessed by the turbine rotors. However, the region with higher velocity deficit (e.g., $U/U_H < 0.6$) from $X/D = 1.1$ to $X/D = 2.2$ in the wake of the CO-DRWT model is clearly larger than the other two cases. This result could be a good explanation for the lowest power output in the CO-DRWT model at $X/D = 2.0$, as shown in Fig. 7. Similarly, the velocity deficit in the CR-DRWT case is found to be slightly higher than that in the SRWT model in the wake region within $-0.2 < Z/D < 0.2$, through the comparison of the areas with high velocity deficit ($U/U_H < 0.6$). However, from the denser contour lines shown in Fig. 8(c), the velocity gradient in the vertical direction is larger than the case shown in Fig. 8(a), indicating a stronger shear stress in the turbine wake of the CR-DRWT model.

Due to the existence of the appended small rotor in the DRWT

designs, the velocity distribution in the region between $X/D = -0.2$ and $X/D = 0.2$ depicts an essential distinction in comparison to those in the SRWT system. As shown in Fig. 8(a), a region with relatively high velocity ($U/U_H > 0.8$) in the near wake behind the SRWT is found to appear right above the turbine nacelle (i.e., in the radial region of $0.05 < Z/D < 0.15$) and is extended up to the downstream location of $X/D = 0.4$. These results could be also found in our previous experimental study on a same wind turbine [17], which are believed to be caused by the poor aerodynamic performance at the blade root sections in the SRWT design. As a result, little to no wind energy from the incoming airflow is harnessed by the rotor blades in this region. Similar flow features were also reported by Hu et al. [25,38] and Wang et al. [17]. As expected, because of the existence of the auxiliary rotor in the DRWT configurations, the velocity in the region between the auxiliary rotor and the main rotor is found to be much less. Obviously, the wind energy in this region is captured and converted to electric power by the small rotor. This could be used for explaining the reason why the isolated DRWT designs could generate more power outputs than the conventional SRWT, as shown in Fig. 6. However, the differentiation of power outputs between the CO- and CR-DRWT models cannot be identified from this analysis because almost the same velocity values in the region between the upwind and downwind rotors are observed from the comparison. Therefore, further study is discussed in the following section of point-wise velocity measurement.

In order to further investigate the turbulent flow in the turbine wakes, the spatial distribution of the primary turbulent kinetic energy production (TKEP) is derived from the measured flow fields, which is defined as below [21]:

$$TKEP = -\overline{u'w'} \times \frac{\partial U}{\partial z} \tag{6}$$

where the term of $-\overline{u'w'}$ is the Reynolds stress calculated from the instantaneous and ensemble-averaged velocity vectors. The flux of TKEP is closely associated with the high shear of the mean velocity in the radial direction and the radial fluxes of momentum (towards the wake center) [47]. This term would indicate the rate of horizontally-averaged mean flow kinetic energy is being lost due to the production of turbulent kinetic energy [48] and is also used to evaluate the flux across horizontally-oriented surfaces, which will play an important role in entraining the high-momentum airflows over the rotational disk to recharge low-momentum airflows in the center of wake for typical wind farms [49].

Fig. 9 illustrates the ensemble-averaged TKEP distributions in the wake flows. It can be seen that most of high levels of TKEP are concentrated in the upper half of the turbine wake, especially in the region of $Z/D > 0.2$. Similar phenomenon was also reported in Chamorro et al. [21,40,50], when they investigated the turbulent flow characteristics in small wind farms by experimental measurements. The TKEP levels are quite small near the rotor blades and gradually develop in the downstream regions because the turbulent mixing is gradually enhanced by the wake development in the region with large radial shear stress in streamwise velocity. On

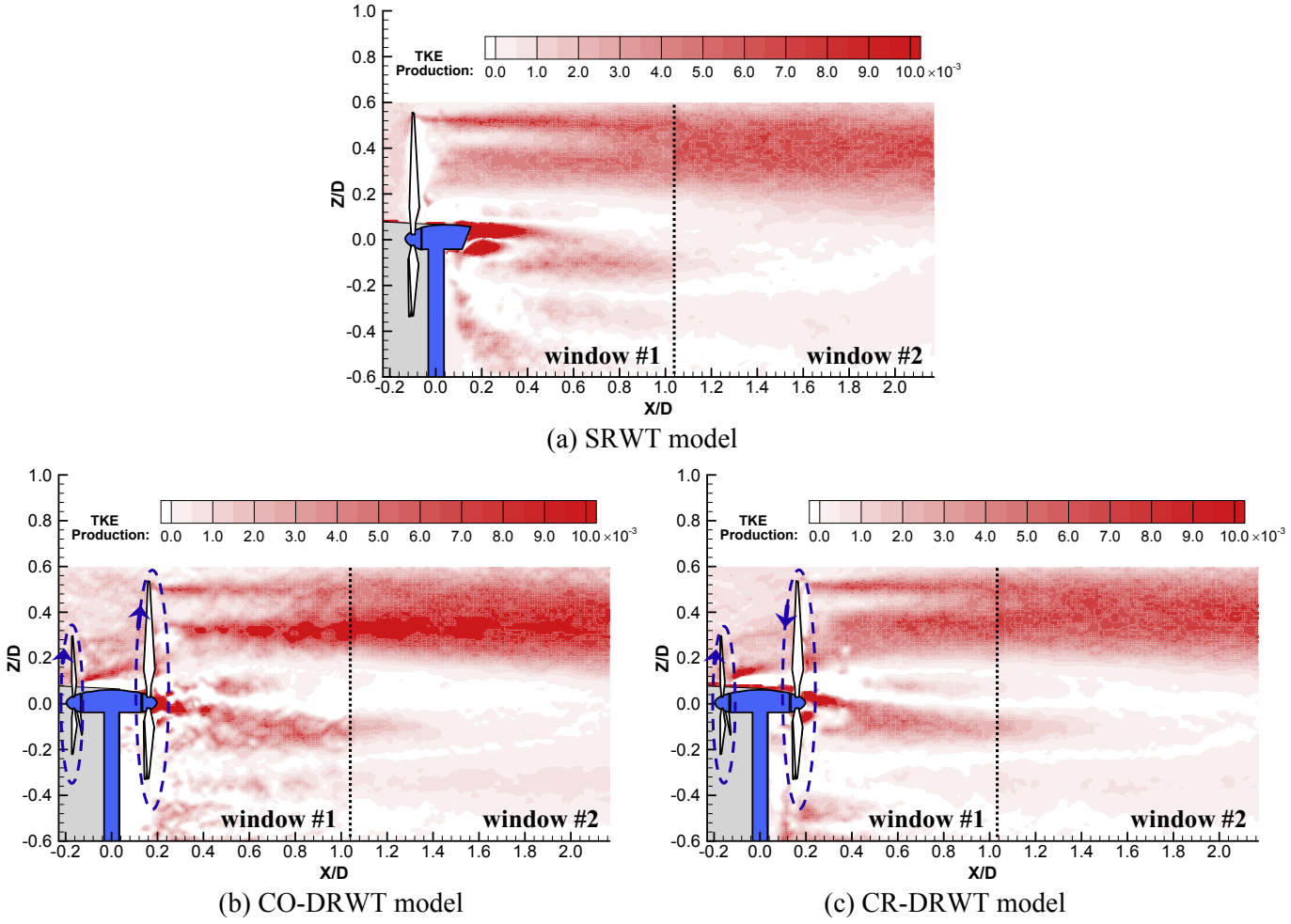

Fig. 9. Turbulence Kinetic Energy Production distributions in the wake flows.

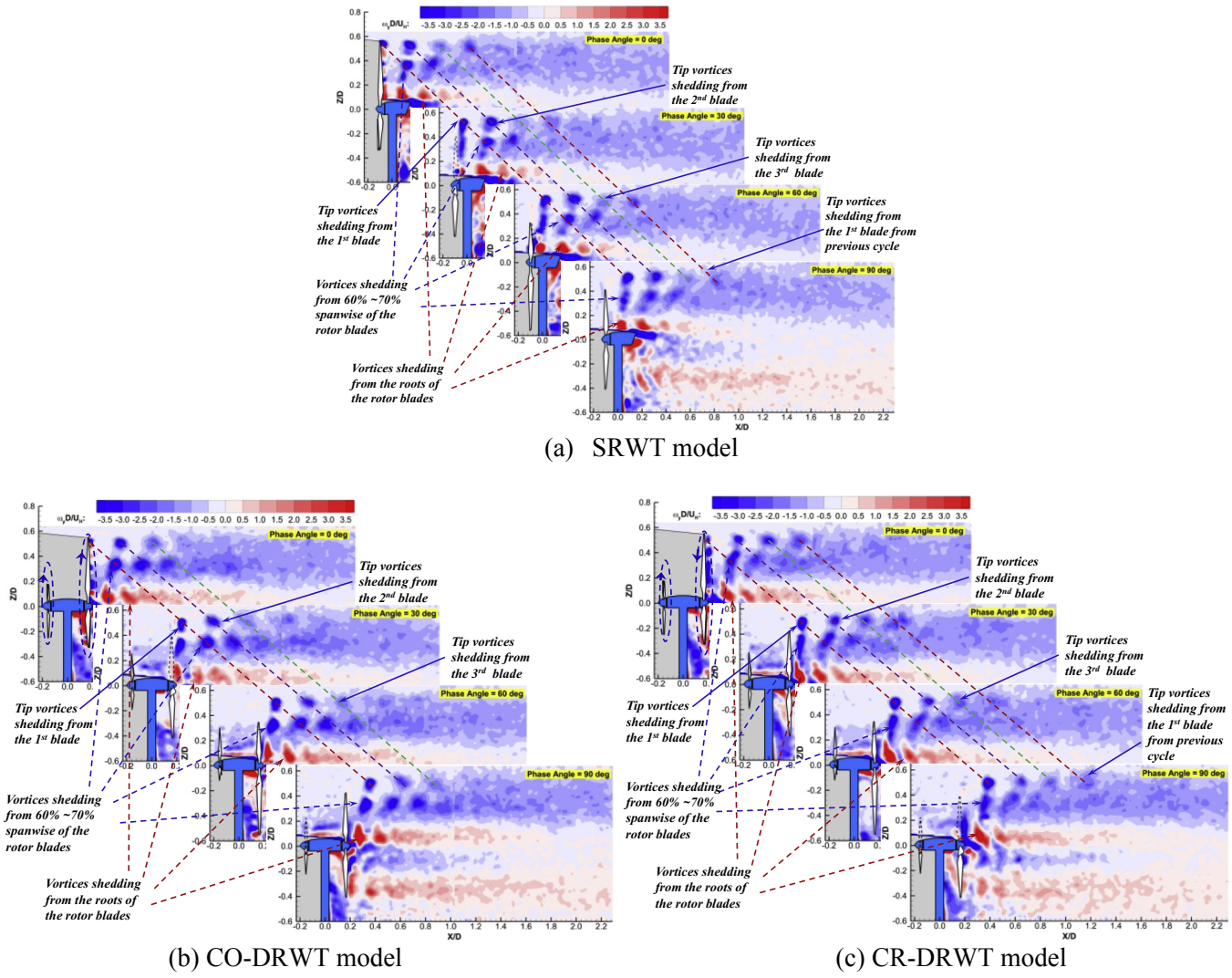

(a) SRWT model

(b) CO-DRWT model

(c) CR-DRWT model

Fig. 10. Phase-locked PIV measurement results in the wake flows.

the other side, very low TKEP values are found at the lower half of the turbine wake, where the velocity gradient is relatively small as shown in Fig. 8. However, a small region behind the turbine nacelle is also found with very high levels of TKEP, which is much larger in the SRWT case in comparison to those in the DRWT cases. From the comparison, the TKEP values in the wake of the DRWT models are significantly higher than that in the SRWT case, especially in the case of CO-DRWT model, indicating more high-momentum airflows would be entrained into the turbine wake regions. This would imply a shorter distance is needed for recovering the velocity deficits in the wake of the DRWT systems. Obviously, the highest TKEP is found to be occurred in the wake of the CO-DRWT model, which is believed to be induced by the strong wake interferences from the auxiliary and main rotors. Therefore, the velocity recovery in the wake of the CO-DRWT system would be faster than those in the other two models. This could be the reason to explain the results shown in Fig. 7, where the power output from the CO-DRWT model is 6.8% lower than the SRWT model at the location of $X/D = 2.0$ but is 12.4% higher at the location of $X/D = 4.0$. Similarly, the TKEP values in the CR-DRWT system are found to be slightly higher when compared with the SRWT model, also corresponding with a smaller increase in power generation as shown in Fig. 7. As a result, the faster recovery of the velocity deficits in the far wake (e.g., $X/D > 2.0$) behind the dual-rotor configurations, especially in the CO-DRWT concept, are believed to be closely in relation to the generation of more complicated vortex structures and enhanced turbulent mixing due to the existence of the auxiliary rotor.

In addition to the ensemble-averaged PIV measurement results shown above, the phase-locked PIV measurements were also performed in order to discover the evolution process of the unsteady vortices in the turbine wakes. As mentioned above, the zero phase angle of the pre-labeled blade was defined when the blade at the most upward position. The tachometer, shown in Fig. 4, was used to capture the rotational speed via the signals generated by the periodic pulses received from the rotating blade. Then, the laser and the camera systems were triggered by these signals when the position of rotor blade was assumed to be frozen at a certain time step. The vorticity in the vertical PIV measurement plane (ω_y) is defined as follows:

$$\omega_y = \frac{\partial w}{\partial x} - \frac{\partial u}{\partial z} \tag{7}$$

It is used to quantify the unsteady turbulent characteristics such as the formation, shedding, breakdown and dissipating processes of tip and root vortices in the wake flows.

Fig. 10 presents the normalized vorticity ($\omega_y D/U_H$) distributions in the vertical central plane of the SRWT and DRWT models. As expected, the wake flows behind these miniature wind turbines are

very complex, and multiple unsteady vortices are generated in different orientations and sizes from the rotor blades, nacelles and towers. It should be mentioned that in this phase-locked measurement, the increment of the blade phase angle is 15°, but there are only four phase angles (i.e., $\theta = 0.0°$, 30.0°, 60.0°, 90.0°) presented in this paper for conciseness. The differences on the evolution of the unsteady turbulent structures in the wake flows behind these three model turbines can be clearly identified from this comparative study. As shown in Fig. 10, vortices are clearly seen in the upper half of the turbine wakes, in comparison with those in the lower half of the turbine wake. This is because of the existence of the towers and nacelles, the airflows in the lower half turbine wake are essentially affected by these static components in the vertical PIV measurement plane, instead of being determined by the rotating blades as shown in the upper half wake region. Thus, the primary distinction in the turbine wakes is seen from the upper half wake region. In the PIV measurements, the tip vortices are induced from the tip of the main rotor blades at the phase angle of $\theta = 0.0°$. With the phase angle increases, the tip vortices are observed to shed from the tip of the blades and align sequentially with the tip vortices shedding from the other main rotor blades in the wake regions. The shape and strength of the tip vortices in the wakes of SRWT and CR-DRWT configurations are found to be quite similar and the vortex structures can be clearly identified from the previous cycle in the wake regions. While in the case of CO-DRWT, the strength of the tip vortices are smaller and these vortices are found to be dissipated faster than those in the other two cases. Recall the least power output generated from the main rotor in CO-DRWT design shown in Fig. 6, which could be incurred by the smaller rotational speed of the main rotor induced by the interaction between upwind and downwind turbines. As a result, the tip vortices are not less strong and rapidly dissipated when compared with the other two cases.

Apart from the tip vortices, an additional series of vortices with high strength are also observed to be generated from 60%–70% spanwise of the main rotor blades. Similar vortex structures were also reported in the studies of Whale et al. [39] and Hu et al. [38]. As can be seen from Fig. 10, they are found to move outward in the wake of the SRWT model but slightly move inward in the wake of the CO-DRWT system, which may indicate a severe wake interference occurring between the upwind and downwind rotors in the co-rotating design. In the wake of CR-DRWT model, however, they are found to be elongated in vertical direction and dissipated rapidly in the wake compared with the other two cases. As a result, such a significant discrepancy in the dual-rotor designs is believed to be closely associated with the relative rotating direction of the upwind and downwind rotors. It indicates that the co-rotating configuration would strength the vortices but the counter-rotating one would change the shape of them in the wakes behind 60%–70% span of the main rotor blades. Recall the TKE production presented in Fig. 9, this could be the reason for the higher TKE production in the turbine wakes of dual-rotor designs, especially in the CO-DRWT design. It could also explain the higher aerodynamic forces in DRWT systems shown in Fig. 5, because stronger wake interferences are observed due to the existence of the auxiliary rotor. In addition, the unsteady vortex structures are generated from the blade root regions with a circular shape and shed downstream periodically in the measurement of SRWT model. However, they are stretched in vertical direction in the wake of CO-DRWT system and tilted in the wake of CR-DRWT design. This result clearly illustrates that, the auxiliary rotor installed in the dual-rotor designs would significantly affect the flow characteristics in the region of $0.1 < Z/D < 0.4$, which have essential impacts on the power outputs as well as aerodynamic forces for the upstream turbines and also on the wake mixing in the downstream regions.

As mentioned above, a cobra anemometry probe was also employed in the current experiment to obtain the point-wise velocity distributions in the far wake regions to supplement the data in the near wake regions measured by the PIV system. Fig. 11 presents the vertical profiles of the normalized streamwise velocity at the downstream locations of $X/D = 2.0$, 4.0, 6.0, 8.0 and 12.0, respectively, behind the SRWT and DRWT systems. Besides, the velocity profiles of the freestream (i.e., without wind turbines installed at the test locations) are also provided in these plots for comparison. Since a large portion of kinetic energy from the incoming wind is harnessed by turbines when airflows passing through the rotating blades, remarkable velocity deficits can be found in the wakes, which is identical to the findings in the near wake regions shown in the PIV measurements. At $X/D = 2.0$, the incoming flow is found to decelerate more significantly in the root regions of the main rotor blades (e.g., $-0.3 < Z/D < 0.3$) for the DRWT models. This is because the upwind small rotors harvest an extra portion of wind energy in this region and cause larger velocity deficits in the near wakes. The result shown in Fig. 11(a) coincides with the PIV measurement results given in Fig. 8, where the largest velocity deficit is found in the wake of the CO-DRWT. The velocity deficit in the CR-DRWT within the region of $-0.3 < Z/D < 0.3$ also shows a higher level than that in the SRWT case, but an opposite situation is observed beyond this region, where a less velocity deficit can be identified. Therefore, the results illustrated in Fig. 11(a) agree well with the power outputs for a same wind turbine placed at the location of $X/D = 2.0$.

According to the findings shown in Fig. 9, higher TKE production levels would indicate a faster velocity recovery in the turbine wakes. As a result, the velocity distributions shown in Fig. 11(b) depicts a remarkable distinction with the profiles shown in Fig. 11(a). The streamwise velocity profiles in the DRWT cases are recovered to significantly higher levels compared to that in the SRWT model. This is believed to be strongly associated with the higher TKE production levels in the wakes, which indicate more intensive turbulent mixing in the wake region of $2.0 < X/D < 4.0$ to promote a faster vertical transport process of the high-momentum flows entraining from the region above turbine wakes to recharge the low-momentum wake flows. Similar results were also reported in the studies of by Wu and Porte-Agel [47], and Calaf et al. [51]. It implies that the airflows in the wakes of the DRWT designs would become more energetic and higher power generation can be expected for the wind turbine placed at the downstream location of $X/D = 4.0$. Meanwhile, the maximum velocity difference between the DRWT and SRWT models is observed at $X/D = 4.0$ among the all measurement locations, which also coincides with the measured maximum power enhancement given in Fig. 8. Fig. 11(c) depicts the streamwise velocity distributions at $X/D = 6.0$, where much smaller difference between the DRWT and SRWT models can be identified in comparison to those at the location of $X/D = 4.0$. It reveals that, the benefits of promoting the velocity recovery in the wake of DRWT designs are found to be gradually diminished. But the velocity measured in the wake of the SRWT model are still observed to be lower than those in the wakes of the DRWT models, especially at the lower half turbine wake. It agrees well with the power outputs presented in Fig. 8 at the location of $X/D = 6.0$. When the downstream turbine is placed at $X/D = 8.0$, the velocity deficits shown in Fig. 11(d) are found to be further recovered in comparison to the freestream profile. The differences between the DRWT cases are observed to become small, which also correspond with the power measurements shown in Fig. 7. It indicates that the effect from the rotational direction of upwind and downwind rotors disappears from $X/D = 6.0$ since the velocity profiles at $X/D = 6.0$ and $X/D = 8.0$ almost keep the same. The benefits from the dual-rotor designs for promoting the turbulent mixing and enhancing a

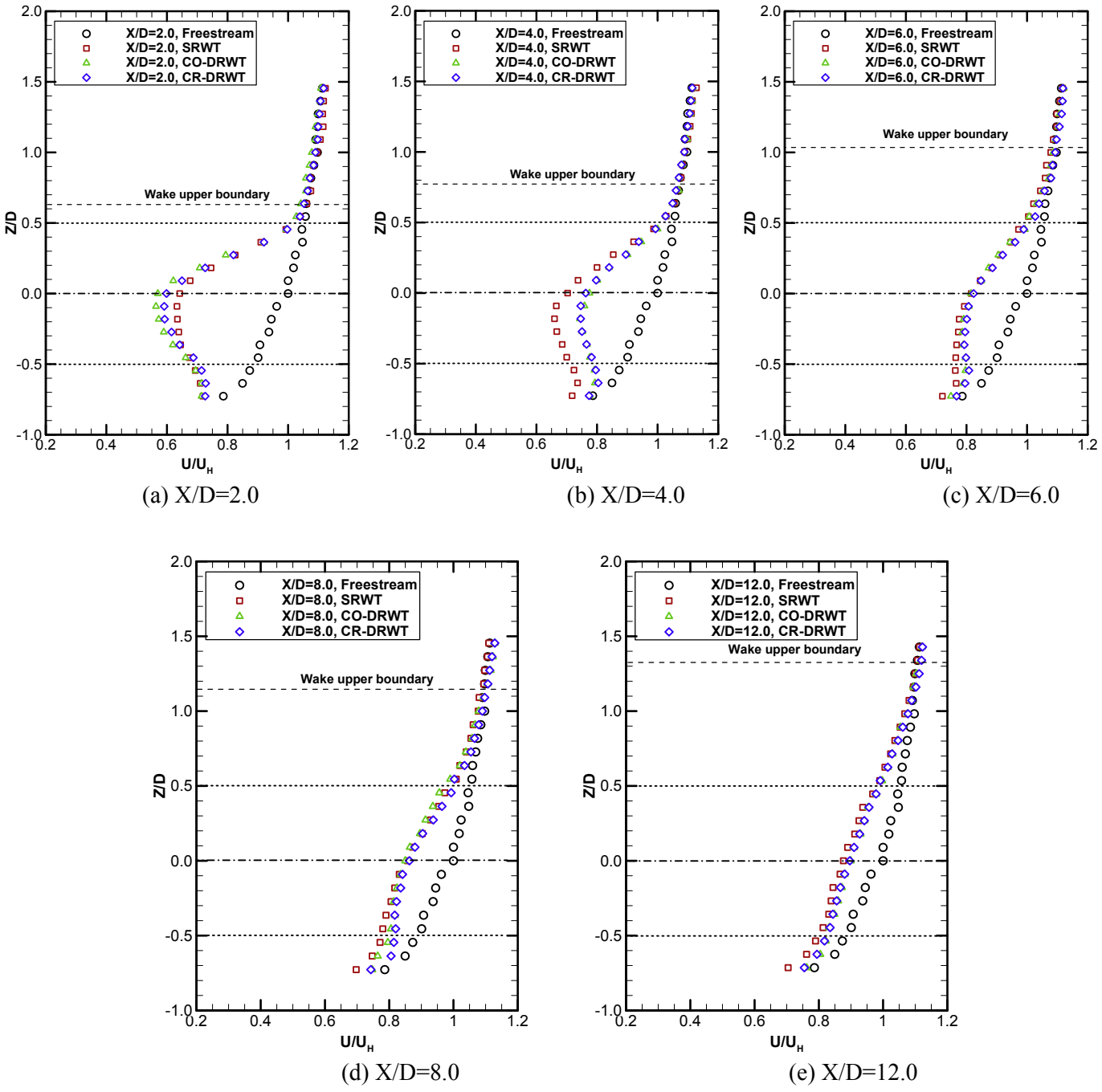

Fig. 11. Vertical profiles of streamwise velocity at variant locations in wake flows.

faster velocity recovery would gradually fade away as less velocity differentiation is observed at further downstream locations. Fig. 11(e) illustrates the streamwise velocity profiles at the downstream location of $X/D = 12.0$, where the velocity deficits are still existed. That means a longer distance is required to recover the velocity to the same level with the freestream. According to the findings from Chamorro et al. [21] and Zhang et al. [22], the effects of turbine wake can be extended as far as 20 rotor diameters downstream of the turbine rotational disk. Besides, the upper boundaries of the turbine wakes, marked as the long dash lines in the figures, are also plotted for visualizing the development of wake regions. It can be seen clearly that, the upper boundaries of the wakes behind the measured three wind turbine models are found to be almost identical since they are primarily determined by the big rotors.

As mentioned in Fig. 6, the CR-DRWT model could harness more wind energy from the same incoming airflows than that of CO-DRWT, when both of them operate in isolated conditions. However, the physics behind this distinction still haven't discovered in the previous analysis. As suggested by Ozbay et al. [29] and Yuan et al. [30], the azimuthal (swirling) velocity could be a significant parameter in the power generation of downwind turbines. They stated that the azimuthal velocity induced from the upwind rotor in counter-rotating design could be utilized by the downwind rotor, which contributes a higher power output in the downwind turbine. Fig. 12 presents the vertical profiles of azimuthal (swirling) velocity at the downstream locations of $X/D = 0.5$, 1.0 and 2.0, respectively.

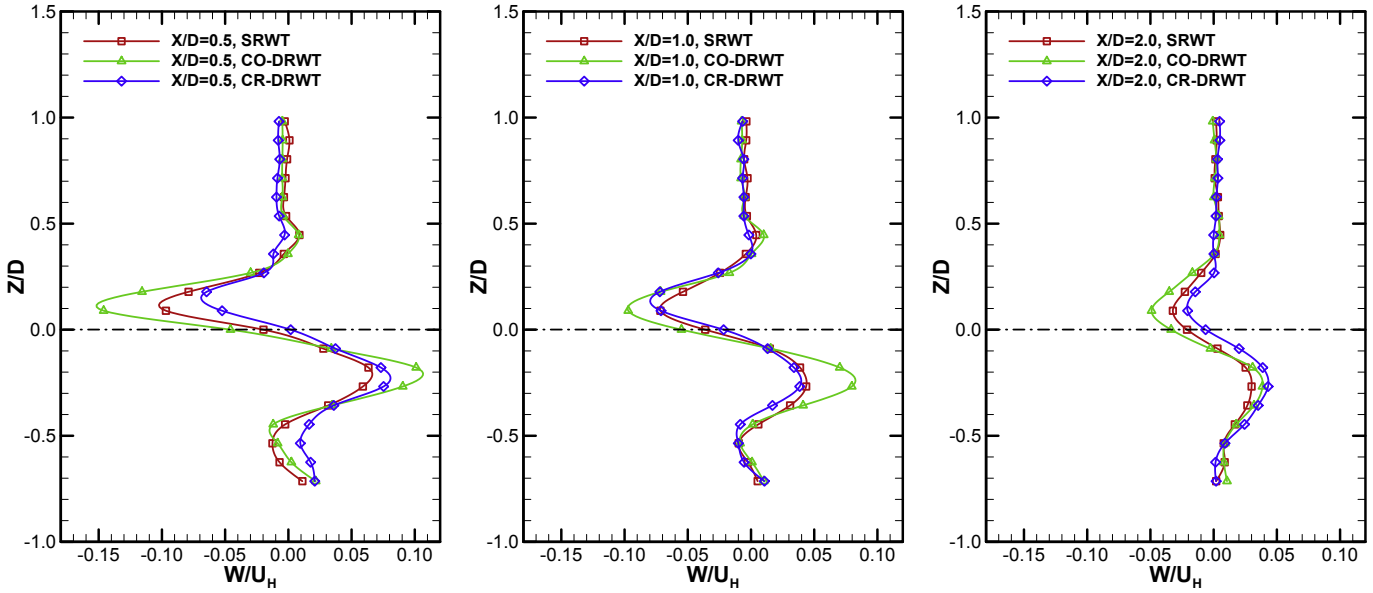

Fig. 12. Azimuthal (swirling) velocity profiles in the wakes behind the SRWT and DRWT models.

They are also measured by the cobra probe that is placed in the wake regions behind the SRWT and DRWT models. As expected, they are found to be significant within the region of $-0.3 < Z/D < 0.3$ in comparison to those outside of this region, which is induced by the rotational effect of turbine rotors. Therein, the azimuthal velocity in the wake behind the CR-DRWT model is observed to be the least among the measured cases, especially in the upper half wake. It is believed that a large portion of the kinetic energy from azimuth velocity is harvested by the downwind rotor, indicating a better capability for harnessing wind energy from the same incoming wind profile through the counter-rotating configuration. In contrast, the azimuthal velocity in the wake of the CO-DRWT case would be augmented by the downwind rotor, causing a proportion of wind energy would escape and be wasted in the turbine wake. This result could be used to explain why the counter-rotating configuration has a better power generation in comparison to that of the co-rotating design. Furthermore, the magnitudes of azimuthal velocity are found to be gradually reduced as the distance increases (i.e., from $X/D = 0.5$ to $X/D = 2.0$). It also reveals that the effect of rotational direction would be gradually decreased and faded away in the further downstream locations.

3.4. Conclusion

An experimental study was conducted to investigate the power and force performances as well as the wake characteristics of a novel dual-rotor wind turbine (DRWT) with co- and counter-rotating configurations, in comparison with those of a traditional single-rotor wind turbine (SRWT). In addition to measuring the power performances and the aerodynamic forces acting on the DRWT and SRWT models, a high-resolution PIV system was employed to perform both ensemble-averaged and phase-locked measurements to characterize the turbulent flow structures and the evolution of the unsteady tip and root vortices in the wakes behind the model turbines. The power outputs of a same SRWT placed at variant downstream locations and the point-wise velocities measured by a cobra probe were used to quantify the wake recovery characteristics behind the DRWT models from near to far wake regions. The measurement results reveal clearly that the DRWT designs have better capabilities of harvesting more wind energy when operated both in isolated and wind farm scenarios.

The main conclusions derived from the present study can be summarized as follows:

1. The time-averaged aerodynamic forces and their standard deviations in the CO-DRWT and CR-DRWT systems were measured to be higher than those of the SRWT case. While the CO-DRWT model has a higher wind loads than those in the CR-DRWT design, which is believed to have a stronger wake interference between the upwind and downwind rotors. This would indicate that rotational direction of the dual-rotor configurations has significant impact on the wind loads on the turbines.
2. The power measurement results illustrate that 7.2% and 1.8% enhancements were found in the CR-DRWT and CO-DRWT models when operated in isolated condition, respectively, in comparison to that in the SRWT model. This is believed due to the swirling velocity induced by the upwind rotor is utilized by the downwind rotor in the CR-DRWT configuration.
3. The largest velocity deficit was found to be existed in the near wake of CO-DRWT case, which may account for the lowest power output of the downstream turbine sited at the downstream location of $X/D = 2.0$. The high-momentum airflows over the turbine nacelle (in the 25% root region of main rotor) were found to be significantly harnessed because a portion of wind energy was harvested by the auxiliary rotor, which could be used for explaining the reason why the DRWT configurations produce more power than the conventional SRWT due to root losses.
4. The primary term of turbulent kinetic energy production (TKEP) was found to be highest in the wake region of the CO-DRWT, which indicated a faster process of entraining the high-momentum airflow from the region above the rotational disk to recharge the downstream turbine wakes and brought a rapid streamwise velocity recovery in the wake regions.
5. The phase-locked measurements presented the evolution process of blade tip, root and mid-section vortices and the unsteady turbulent structures generated from the nacelles as well as

towers in the turbine wakes. They revealed that the tip vortices in the CO-DRWT case have smaller strength and would dissipate faster in the wake region. However, the vortices shedding from approximately 60%–70% span of the main rotor are found to be much stronger than the other two models, which is believed to be induced by the wake interaction between the upwind auxiliary and downwind main rotors.

6. The power outputs for a SRWT model placed at downstream locations showed that the maximum power enhancement of 15.4% can be achieved at the location of $X/D = 4.0$ in the wake of CR-DRWT, in comparison to that in the conventional SRWT model. The fastest velocity recovery speed can be found in the wake of the CO-DRWT model within the range of $X/D = 2.0$ and $X/D = 4.0$. This would reveal that the wake losses are significantly mitigated in the turbine wake of DRWT models, especially in the CO-DRWT case.
7. The measurements of swirling velocity also confirmed that the counter-rotating design could harvest the azimuthal velocity induced from the upwind small rotor and hence contribute a higher power output than that of co-rotating design when they operated in isolated condition.

Based on the findings derived from the present study, we believe that the dual-rotor designs are capable of reducing the losses incurred in the root region and enhancing the turbulent mixing in the wake, but more comprehensive studies should be performed to confirm the flow characteristics in large-scale wind turbines. However, due to the limitation of low Reynolds number used in the present study, more detailed flow physics should be investigated at a much higher Reynolds number for a more comprehensive analysis.

Acknowledgements

The funding support from the Iowa Energy Center with Grant No. 14-008-OG and National Science Foundation (NSF) with Grant Numbers of CBET-1133751 and CBET- 1438099 is gratefully acknowledged.

References

[1] Burton T, Jenkins N, Sharpe D, Bossanyi E. Wind energy handbook. second ed. Wiley; 2011.
[2] Rosenberg A, Selvaraj S, Sharma A. A novel dual-rotor turbine for increased wind energy capture. J Phys Conf 2014;524. https://doi.org/10.1088/1742-6596/524/1/012078.
[3] Sharma A, Frere A. Diagnosis of aerodynamic losses in the root region of a horizontal Axis wind turbine. 2010. General Electric Global Research Center Internal Report.
[4] Global wind Statistics-2016. 2017.
[5] Barthelmie RJ, Rathmann O, Frandsen ST, Hansen KS, Politis E, Prospathopoulos J, et al. Modelling and measurements of wakes in large wind farms. J Phys Conf 2007;75. https://doi.org/10.1088/1742-6596/75/1/012049.
[6] Vermeer LJ, Sørensen JN, Crespo A. Wind turbine wake aerodynamics. Prog Aero Sci 2003;39:467–510. https://doi.org/10.1016/S0376-0421(03)00078-2.
[7] Varshney K. Characteristics of helical tip vortices in a wind turbine near wake. Theor Appl Climatol 2013;111:427–35. https://doi.org/10.1007/s00704-012-0672-4.
[8] Krogstad P-A, Adaramola MS. Performance and near wake measurements of a model horizontal axis wind turbine. Wind Energy 2012;15:743–56. https://doi.org/10.1002/we.
[9] Hashemi-Tari P, Siddiqui K, Refan M, Hangan H. Wind tunnel investigation of the near-wake flow dynamics of a horizontal Axis wind turbine. J Phys Conf 2014;524, 012176. https://doi.org/10.1088/1742-6596/524/1/012176.
[10] Gao X, Hu J, Wang ZQ. PIV experiment on near wake flow of horizontal Axis wind turbine. Adv Mater Res 2013;718–720:1811–5. https://doi.org/10.4028/www.scientific.net/AMR.718-720.1811.
[11] Zhong H, Du P, Tang F, Wang L. Lagrangian dynamic large-eddy simulation of wind turbine near wakes combined with an actuator line method. Appl Energy 2015;144:224–33. https://doi.org/10.1016/j.apenergy.2015.01.082.
[12] Zhang W, Markfort CD, Porté-Agel F. Near-wake flow structure downwind of a wind turbine in a turbulent boundary layer. Exp Fluid 2011;52:1219–35. https://doi.org/10.1007/s00348-011-1250-8.
[13] Jimenez A, Crespo A, Migoya E, Garcia J. Advances in large-eddy simulation of a wind turbine wake. J Phys Conf 2007;75. https://doi.org/10.1088/1742-6596/75/1/012041.
[14] Yang X, Howard KB, Guala M, Sotiropoulos F. Effects of a three-dimensional hill on the wake characteristics of a model wind turbine. Phys Fluid 2015;27. https://doi.org/10.1063/1.4907685.
[15] Lignarolo LEM, Mehta D, Stevens RJAM, Yilmaz AE, van Kuik G, Andersen SJ, et al. Validation of four LES and a vortex model against stereo-PIV measurements in the near wake of an actuator disc and a wind turbine. Renew Energy 2016;94:510–23. https://doi.org/10.1016/j.renene.2016.03.070.
[16] Abdulqadir SA, Iacovides H, Nasser A. The physical modelling and aerodynamics of turbulent fl ows around horizontal axis wind turbines. Energy 2017;119:767–99. https://doi.org/10.1016/j.energy.2016.11.060.
[17] Wang Z, Tian W, Ozbay A, Sharma A, Hu H. An experimental study on the aeromechanics and wake characteristics of a novel twin-rotor wind turbine in a turbulent boundary layer flow. Exp Fluid 2016;57:1–17.
[18] Adaramola MS, Krogstad P-Å. Experimental investigation of wake effects on wind turbine performance. Renew Energy 2011;36:2078–86. https://doi.org/10.1016/j.renene.2011.01.024.
[19] Barthelmie RJ, Jensen LE. Evaluation of wind farm effi ciency and wind turbine wakes at the Nysted offshore wind farm. Wind Energy 2010;13:573–86. https://doi.org/10.1002/we.
[20] Hansen KS, Barthelmie RJ, Jensen LE, Sommer A. The impact of turbulence intensity and atmospheric stability on power deficits due to wind turbine wakes at Horns Rev wind farm. Wind Energy 2012:183–96. https://doi.org/10.1002/we.
[21] Chamorro LP, Porté-Agel F. Effects of thermal stability and incoming boundary-layer flow characteristics on wind-turbine wakes: a wind-tunnel study. Boundary-Layer Meteorol 2010;136:515–33. https://doi.org/10.1007/s10546-010-9512-1.
[22] Zhang W, Markfort CD, Porté-Agel F. Wind-turbine wakes in a convective boundary layer: a wind-tunnel study. Boundary-Layer Meteorol 2013;146:161–79. https://doi.org/10.1007/s10546-012-9751-4.
[23] Li Q, Murata J, Endo M, Maeda T, Kamada Y. Experimental and numerical investigation of the effect of turbulent in flow on a Horizontal Axis Wind Turbine (Part I : power performance). Energy 2016;113:713–22. https://doi.org/10.1016/j.energy.2016.06.138.
[24] Li Q, Murata J, Endo M, Maeda T, Kamada Y. Experimental and numerical investigation of the effect of turbulent inflow on a Horizontal Axis Wind Turbine (part II: wake characteristics). Energy 2016;113:1304–15. https://doi.org/10.1016/j.energy.2016.08.018.
[25] Tian W, Ozbay A, Hu H. Effects of incoming surface wind conditions on the wake characteristics and dynamic wind loads acting on a wind turbine model. Phys Fluid 2014;26. https://doi.org/10.1063/1.4904375.
[26] Newman BG. Multiple actuator-disc theory for wind turbines. J Wind Eng Ind Aerod 1986;24:215–25.
[27] Lee S, Kim H, Lee S. Analysis of aerodynamic characteristics on a counter-rotating wind turbine. Curr Appl Phys 2010;10:S339–42. https://doi.org/10.1016/j.cap.2009.11.073.
[28] Lee S, Kim H, Son E, Lee S. Effects of design parameters on aerodynamic performance of a counter-rotating wind turbine. Renew Energy 2012;42:140–4. https://doi.org/10.1016/j.renene.2011.08.046.
[29] Ozbay A, Tian W, Hu H. Experimental investigation on the wake characteristics and aeromechanics of dual-rotor wind turbines. J Eng Gas Turbines Power 2015;138, 042602. https://doi.org/10.1115/1.4031476.
[30] Yuan W, Tian W, Ozbay A, Hu H. An experimental study on the effects of relative rotation direction on the wake interferences among tandem wind turbines. Sci Chin Phys Mech Astron 2014;57:935–49. https://doi.org/10.1007/s11433-014-5429-x.
[31] Barthelmie RJ, Jensen LE. Evaluation of wind farm efficiency and wind turbine wakes at the Nysted offshore wind farm. Wind Energy 2010;13:573–86. https://doi.org/10.1002/we.408.
[32] Jain P. Wind energy engineering. McGraw Hill Professional; 2007.
[33] Hsu S, Meindl E, Gilhousen D. Determining the power law wind profile exponent under near neutral stability condition at sea.pdf. J Appl Meteorol 1994:757–65.
[34] Tong W. Wind power generation and wind turbine design. Wit Press; 2010.
[35] Wang Z, Hu H, Tian W, Ozbay A. An experimental investigation on the wake characteristics behind a novel twin-rotor wind turbine. In: AIAA SciTech conference 2015. AIAA; 2015. https://doi.org/10.1115/1.4031476.
[36] Sarlak H, Nishino T, Martinez-Tossas LA, Meneveau C, Sorensen JN. Assessment of blockage effects on the wake characteristics and power of wind turbines. Renew Energy 2016;93:340–52. https://doi.org/10.1016/j.renene.2016.01.101.
[37] Chamorro L, Arndt R, Sotiropoulos F. Turbulent Flow Properties around a staggered wind farm. Boundary-Layer Meteorol 2011;141:349–67. https://doi.org/10.1007/s10546-011-9649-6.
[38] Hu H, Yang Z, Sarkar P. Dynamic wind loads and wake characteristics of a wind turbine model in an atmospheric boundary layer wind. Exp Fluid 2012;52:1277–94. https://doi.org/10.1007/s00348-011-1253-5.
[39] Whale J, Anderson C, Bareiss R, Wagner S. An experimental and numerical study of the vortex structure in the wake of a wind turbine. J Wind Eng Ind Aerod 2000;84:1–21. https://doi.org/10.1016/S0167-6105(98)00201-3.
[40] Chamorro L, Arndt R, Sotiropoulos F. Turbulent flow properties around a staggered wind farm. Boundary-Layer Meteorol 2011;141.
[41] Medici D, Alfredsson PH. Measurements on a wind turbine wake: 3D effects and bluff body vortex shedding. Wind Energy 2006;9:219–36. https://doi.org/

10.1002/we.156.
[42] Hu H, Wei T, Wang Z. An experimental study on the wake characteristics of dual-rotor wind turbines by using a Stereoscopic PIV technique. In: 34th AIAA applied aerodynamics conference 2016; 2015. https://doi.org/10.2514/6.2016-3128.
[43] Frandsen S, Barthelmie R, Pryor S, Rathmann O, Larsen S, Hojstrup J. Analytical modelling of wind speed deficit in large offshore wind farms. Wind Energy 2006;9:39–53. https://doi.org/10.1002/we.
[44] Kishinami K, Taniguchi H, Suzuki J, Ibano H, Kazunou T, Turuhami M. Theoretical and experimental study on the aerodynamic characteristics of a horizontal axis wind turbine. Energy 2005;30:2089–100. https://doi.org/10.1016/j.energy.2004.08.015.
[45] Barthelmie RJ, Rathmann O, Frandsen ST, Hansen KS, Politis E, Prospathopoulos J, et al. Modelling and measurements of wakes in large wind farms. J Phys Conf 2007;75. https://doi.org/10.1088/1742-6596/75/1/012049.
[46] Barthelmie RJ, Hansen K, Frandsen ST, Rathmann O, Schepers JG, Schlez W, et al. Modelling and measuring flow and wind turbine wakes in large wind farms offshore. Wind Energy 2009;12:431–44. https://doi.org/10.1002/we.348.
[47] Wu Y-T, Porté-Agel F. Atmospheric turbulence effects on wind-turbine wakes: an LES study. Energies 2012;5:5340–62. https://doi.org/10.3390/en5125340.
[48] Calaf M, Meneveau C, Meyers J. Large eddy simulation study of fully developed wind-turbine array boundary layers. Phys Fluid 2010;22. https://doi.org/10.1063/1.3291077.
[49] Newman J, Lebron J, Meneveau C, Castillo L. Streamwise development of the wind turbine boundary layer over a model wind turbine array. Phys Fluid 2013;25. https://doi.org/10.1063/1.4818451.
[50] Chamorro LP, Tobin N, Arndt REA, Sotiropoulos F. Variable-sized wind turbines are a possibility for wind farm optimization. 2013. https://doi.org/10.1002/we.
[51] Calaf M, Meneveau C, Meyers J. Large eddy simulation study of fully developed wind-turbine array boundary layers. Phys Fluid 2010;22, 015110. https://doi.org/10.1063/1.3291077.